Electronic Supplementary Information

Dithienocyclopentadibenzothiophene: A C_{2V}-Symmetric Core for Nonfullerene Acceptors with Tunable Bandgaps

Changquan Tang,[†,‡] Dongdong Cai[†] and Qingdong Zheng*[,†]

[†]State Key Laboratory of Structural Chemistry, and CAS Key Laboratory of Design and Assembly of Functional Nanostructures, Fujian Institute of Research on the Structure of Matter, Chinese Academy of Sciences, 155 Yangqiao Road West, Fuzhou, Fujian 350002, China

[‡]University of Chinese Academy of Sciences, Beijing 100049, China

Instruments and measurements

Absorption spectra were acquired using a Lambda950 UV-vis spectrophotometer. ^{1}H NMR and ^{13}C NMR spectra were obtained from an AVANCE-III (400 MHz, Bruker) spectrometer. High-resolution mass spectra were recorded by using an UHR TOF LC/MS Mass Spectrometer. Thermogravimetric analysis (TGA) was performed on a Netzsch STA 449C under nitrogen with a heating rate of 10 °C·min^{-1}. Energy levels of NFAs were determined by cyclic voltammetry (CV) experiments with a CHI 604E electrochemical workstation at a scan rate of 100 mV s^{-1}. A platinum plate with neat acceptor films, Ag/$AgNO_3$ (0.01 M in anhydrous acetonitrile), and a platinum wire were used as the working electrode, reference electrode and counter electrode, respectively, in a nitrogen-saturated tetrabutylammonium hexafluorophosphate (*n*-Bu_4NPF_6) solution (0.1 M in anhydrous acetonitrile). The onset oxidation potential ($E_{1/2}$ ox) of ferrocene was -0.02 V *versus* Ag/$AgNO_3$ under these conditions. Assuming the absolute energy level of Fc/Fc^+ to be -4.80 eV *versus* vacuum level, thus the HOMO and LUMO energy levels were obtained from the equation of $E_{HOMO/LUMO} = -(E_{ox}/E_{red} + 4.82)$ (eV), where oxidation/reduction potential onsets (E_{ox}/E_{red}) were determined from the position at which the current raised initially from the baseline. The energy levels of frontier molecular orbitals of the investigated

compounds were obtained from density functional theory (DFT) calculations (at B3LYP/6-311G** level in the ground states) using Gaussian 09. AFM images were obtained from a Bruker Nanoscale V station at a tapping mode. Photoluminescence (PL) spectra were recorded by using a Varian Fluorescence spectrophotometer. The pure donor/acceptor films and their blend films were fabricated by spin-coating the donor/acceptor solutions (8 mg mL^{-1} in CB) and the mixture solutions (16 mg mL^{-1} in CB with a D/A weight ratio of 1:1) at 3300 rpm for 60 s, respectively. According to their absorption peaks, the pure donor/acceptor films were excited by the wavelengths of 550 and 650 nm, respectively. And then the blend films were excited by the wavelengths of 550 and 650 nm, respectively, in the same condition. TEM images were recorded by a JEM-2100F. The samples for TEM measurement was prepared by spin-coating the active layer on ITO/PEDOT:PSS (poly(3,4-ethylenedioxythiophene): poly(styrenesulfonate)) substrate, and the substrate were immersed in deionized water to obtain the floated active layers, then transferred the active layer to TEM grids. The thickness of film was determined by a Bruker Dektak XT surface profilometer.

Fabrication and characterization of OSCs

The inverted devices with the structure of ITO/ZnO/active layer/MoO_3/Ag were fabricated as follows: the ITO glass substrates were cleaned sequentially with detergent, deionized water, acetone, and isopropyl alcohol under sonication for 20 min each, and then dried overnight at 75 °C in an oven, followed by a 15-min ultraviolet/ozone treatment. Then, to obtain a ZnO electron transport layer with a thickness of ~30 nm, a ZnO precursor solution (12 mL of 2-methoxyethanol containing 0.6 g of zinc acetate dehydrate and 0.17 g of ethanolamine) were spin-coated onto the ITO substrates at 3000 rpm for 50 s and followed by thermal annealing in an oven at 200 °C for 60 min. Subsequently, the active layer was prepared by spin-coating a chlorobenzene solution of PBDB-T/acceptor mixture (16 mg/mL, 1:1, w/w) onto the ZnO layer at 3300 rpm for 60 s. The thickness of the blend film is ~100 nm determined by a Dektak150 profilometer. Finally, MoO_3 as an anode buffer layer (10 nm) and Ag as a top electrode (100 nm) were deposited with a shadow mask onto the active layer at a vacuum level of 10^{-4} Pa, respectively. The active area of OSCs was 4 mm^2.

Before the device characterization, all devices were encapsulated with epoxy kits (general purpose, Sigma Aldrich) in the glove-box. The density–voltage (*J*-*V*) test was carried out under AM 1.5G irradiation (100 mW cm^{-2}) in air using a Newport Oriel Sol3A simulator. *J*-*V* curves

were recorded by a Keithley 2440 source meter. External quantum efficiency (EQE) spectra of the best-performance devices were obtained from a Newport EQE measuring system.

Measurements of hole and electron mobilities

Space charge limited current model (SCLC) was employed to determine the hole and electron mobilities of the devices by using a diode configuration of ITO/PEDOT:PSS/active layer/Au (for hole) and ITO/ZnO/active layer/Ca/Al (for electron), respectively. The mobilities were obtained by taking the dark current density measurements with an applied voltage range of 0−14 V and fitting the results to the Mott–Gurney relationship.

$$J = \frac{9}{8}\varepsilon_r \varepsilon_0 \mu \frac{V^2}{L^3}$$

where ε_r is the dielectric constant of the organic semiconductor (assumed to be 3 in this work), ε_0 is the free-space permittivity (8.85×10^{-12} F m^{-1}), μ is the mobility, V is the voltage drop across the SCLC device ($V = V_{appl} - V_{bi}$, where V_{appl} is the applied voltage to the device, and V_{bi} is the built-in voltage due to the difference in the work function of two electrodes), and L is the active layer thickness.

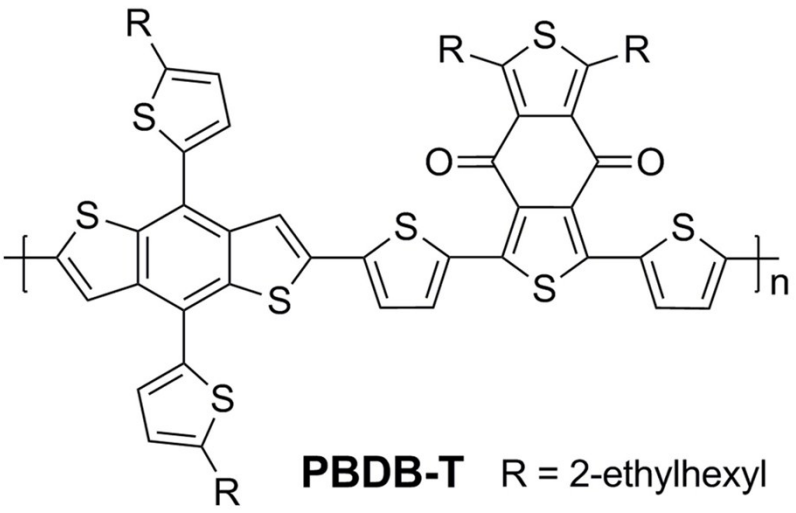

Fig. S1 Chemical structure of PBDB-T.

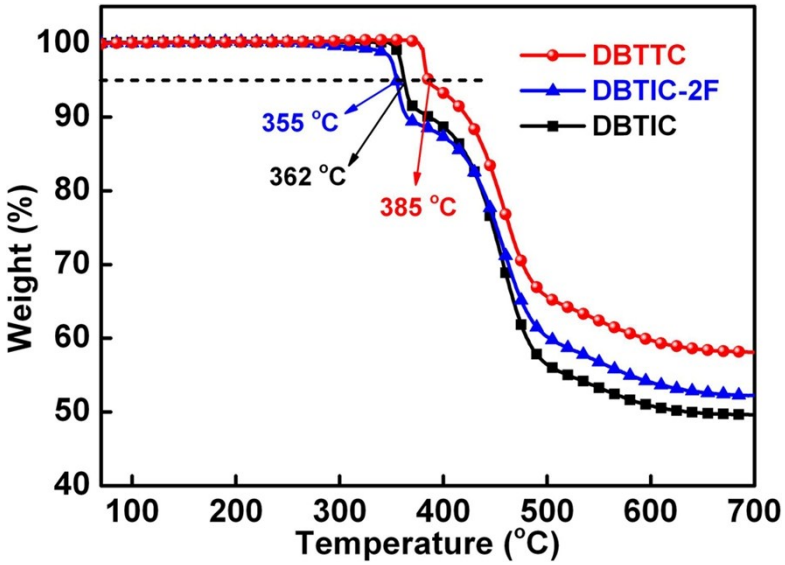

Fig. S2 TGA curves of the three nonfullerene acceptors.

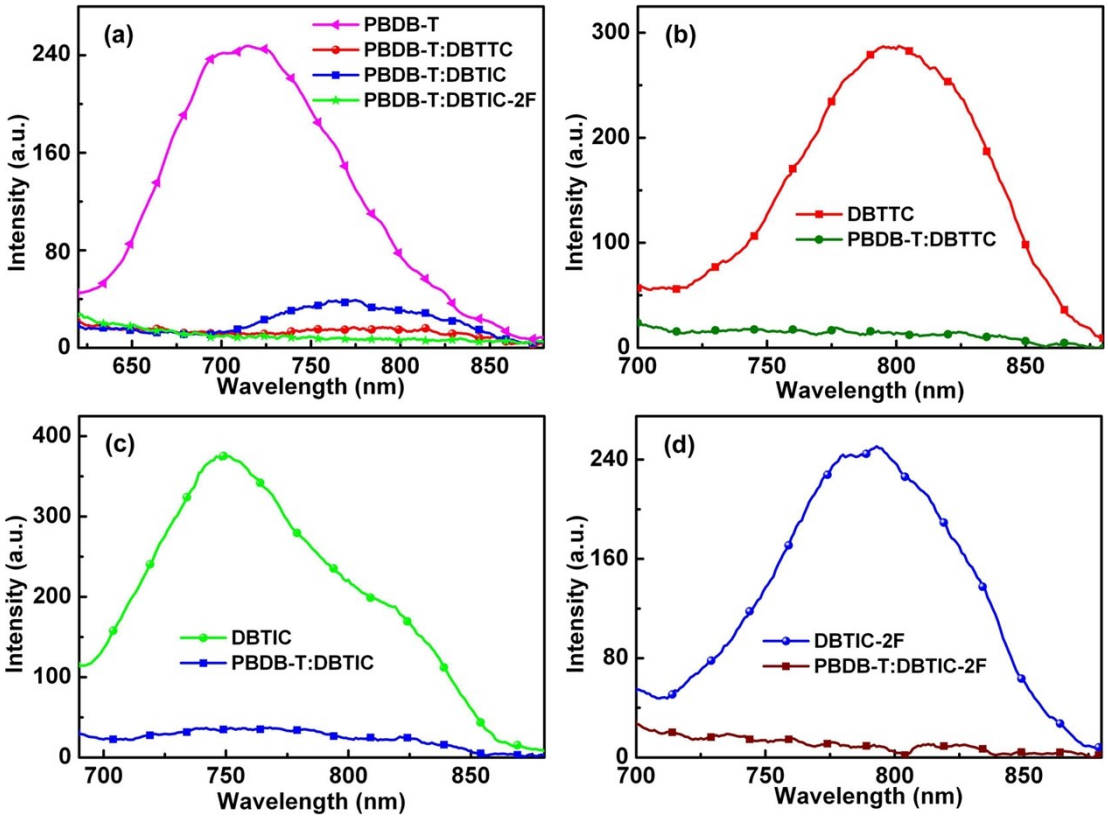

Fig. S3 PL spectra of the pure or blend films based on PBDB-T and the three nonfullerene acceptors: (a) excited at 550 nm; (b, c, d) excited at 650 nm.

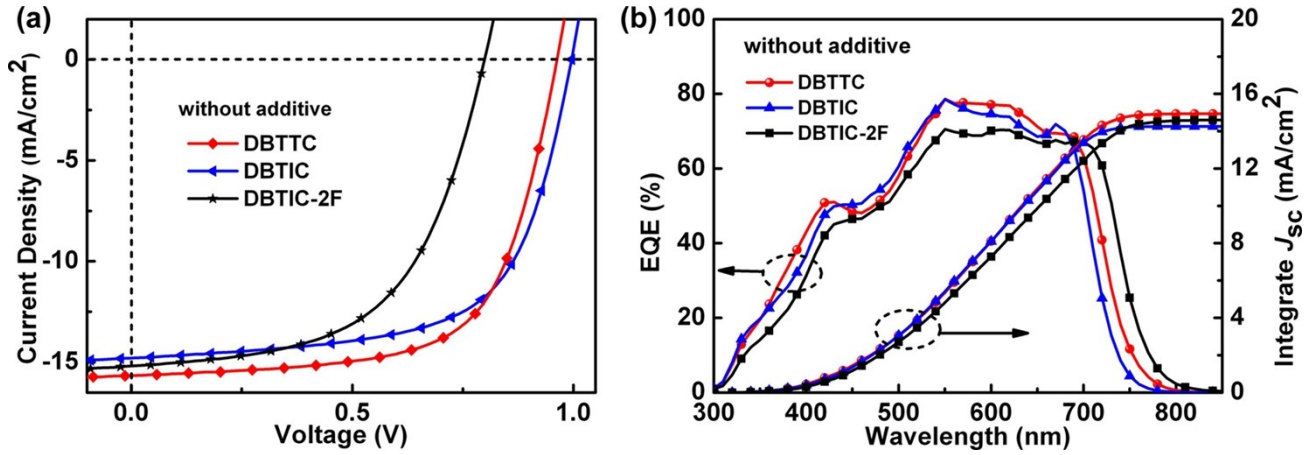

Fig. S4 *J-V* curves (a), EQE spectra and integrated J_{SC} curves (b) of the best-performance devices based on PBDB-T:acceptors without additive.

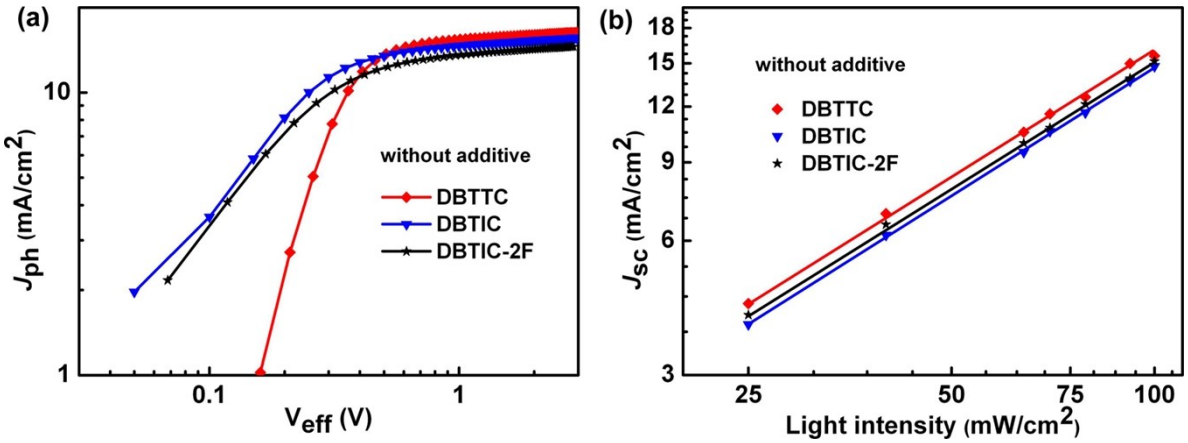

Fig. S5 J_{ph} *versus* V_{eff} (a) and J_{SC} *versus* light intensity (b) for the best devices based on PBDB-T:acceptors without additive.

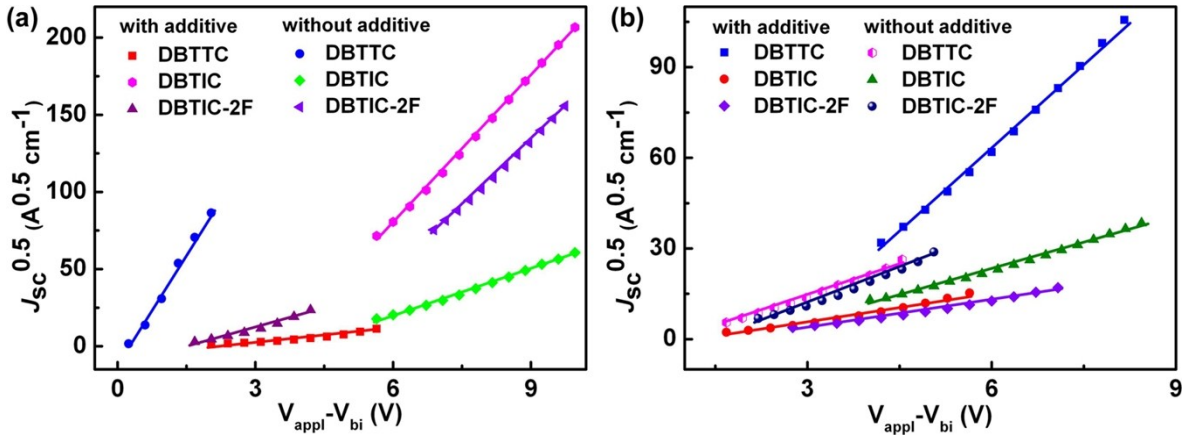

Fig. S6 $J^{1/2}$-*V* characteristics of hole-only (a) and electron-only (b) devices based on PBDB-T:acceptors with or without additive.

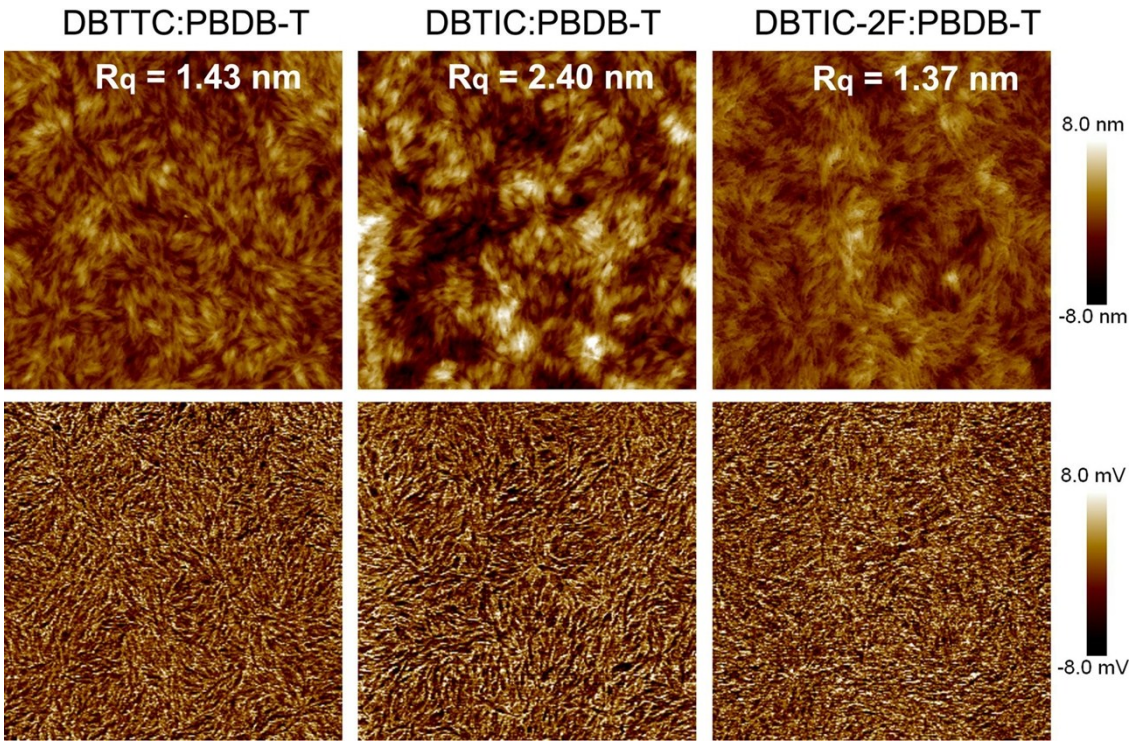

Fig. S7 Tapping mode AFM height (top row) and phase (bottom row) images of blend films for PBDB-T:acceptors without additive.

Table S1 Performance of the devices based on PBDB-T:acceptors with donor/acceptor (D/A) ratio of 1:1 (8 mg/mL of PBDB-T in CB).

Acceptor	Spin-coating speed [rpm]	V_{OC} [V]	J_{SC} [mA cm^{-2}]	FF [%]	PCE[a] [%]
DBTTC	3000	0.971	15.38	63.98	9.55 (9.33 ± 0.19)
DBTIC	3000	0.996	14.85	61.25	9.06 (8.78 ± 0.23)
DBTIC-2F	3000	0.786	13.24	58.94	6.14 (5.83 ± 0.26)

[a] In parentheses are average values based on eight devices.

Table S2 Performance of the devices based on PBDB-T:DBTTC with different D/A ratios (8 mg/mL of PBDB-T in CB).

D/A	Spin-coating speed [rpm]	V_{OC} [V]	J_{SC} [mA cm^{-2}]	FF [%]	PCE[a] [%]
1:0.8	3000	0.970	15.16	61.44	9.04 (8.89 ± 0.13)
1:1	3000	0.971	15.38	63.98	9.55 (9.33 ± 0.19)
1:1.2	3000	0.968	15.01	63.29	9.20 (9.06 ± 0.12)
1:1.4	3000	0.966	14.74	62.24	8.86 (8.67 ± 0.14)

[a] In parentheses are average values based on eight devices.

Table S3 Performance of the devices based on PBDB-T:DBTTC at different spin-coating speeds (D/A = 1:1, 8 mg/mL of PBDB-T in CB).

Spin-coating speed [rpm]	V_{OC} [V]	J_{SC} [mA cm^{-2}]	FF [%]	PCE[a] [%]
2600	0.968	14.81	62.33	8.93 (8.66 ± 0.22)
3000	0.971	15.38	63.98	9.55 (9.33 ± 0.19)
3300	0.962	15.63	65.64	9.88 (9.74 ± 0.11)
3600	0.967	14.91	66.30	9.57 (9.28 ± 0.24)

[a] In parentheses are average values based on eight devices.

Table S4 Performance of the devices based on PBDB-T:DBTTC with different donor concentrations.

Concentration [mg/mL]	Spin-coating speed (rpm)	V_{OC} [V]	J_{SC} [mA cm^{-2}]	FF [%]	PCE[a] [%]
8	3300	0.962	15.63	65.64	9.88 (9.74 ± 0.11)
9	3300	0.958	15.06	63.89	9.44 (9.13 ± 0.26)
10	3300	0.954	15.08	63.37	9.12 (8.97 ± 0.12)

[a] In parentheses are average values based on eight devices.

Table S5 Performance of the devices based on PBDB-T:DBTTC with different additives (D/A = 1:1, 8 mg/mL of PBDB-T in CB, spin-coating speed at 3300 rpm).

Additive [v/v]	V_{OC} [V]	J_{SC} [mA cm^{-2}]	FF [%]	PCE[a] [%]
0.3% DIO	0.980	15.47	67.28	10.21 (10.03 ± 0.14)
0.3% CN	0.955	15.51	68.15	10.09 (9.86 ± 0.18)
0.3% DPE	0.972	16.54	62.33	10.03 (9.74 ± 0.25)
0.5% DIO	0.962	15.37	66.47	9.83 (9.65 ± 0.14)
0.5% CN	0.959	14.80	69.49	9.86 (9.70 ± 0.13)
0.5% DPE	0.979	15.82	59.34	9.12 (8.87 ± 0.20)
0.3% DIO, 0.3% CN	0.970	15.60	68.38	10.35 (10.13 ± 0.19)
0.3% DPE, 0.3% CN	0.959	16.77	65.02	10.46 (10.21 ± 0.21)
0.3% DPE, 0.3% DIO	0.981	15.93	66.60	10.40 (10.18 ± 0.17)
0.3% DIO, 0.3% CN, 0.3% DPE	0.972	17.25	67.04	11.25 (11.08 ± 0.12)

[a] In parentheses are average values based on eight devices.

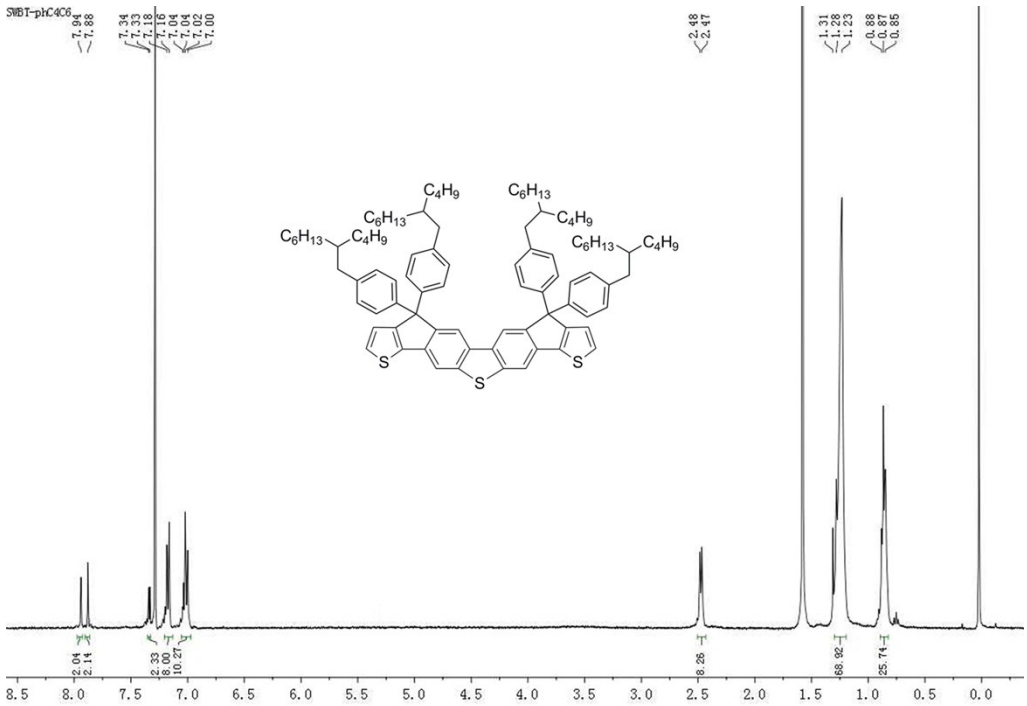

Fig. S8 ^{1}H NMR spectrum of compound **DTCDBT**.

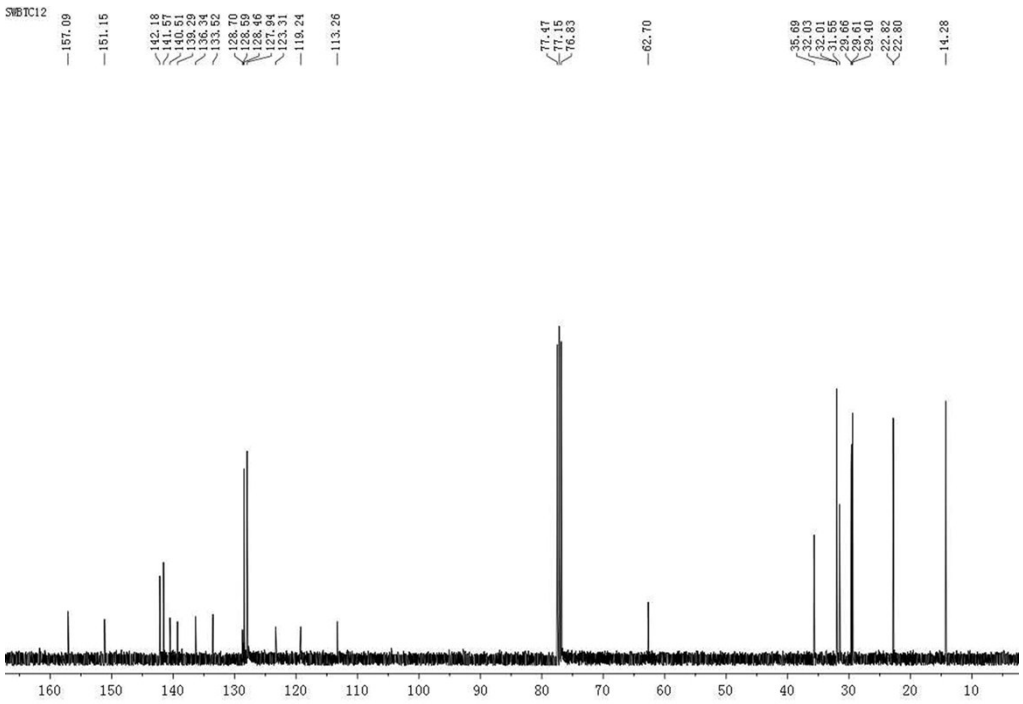

Fig. S9 ^{13}C NMR spectrum of compound **DTCDBT**.

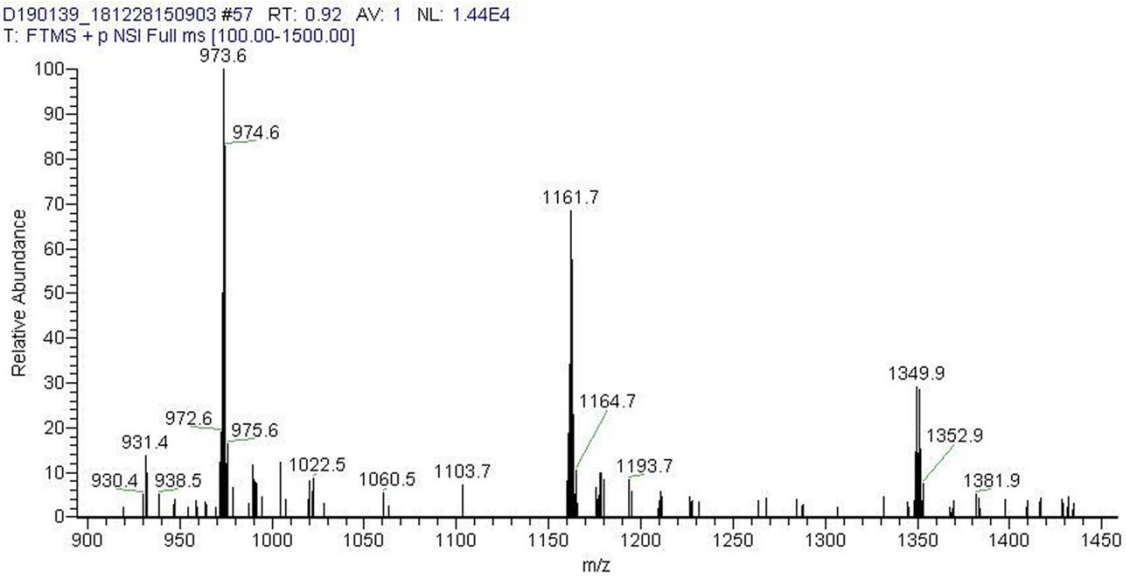

Fig. S10 MS spectrum of compound **DTCDBT**.

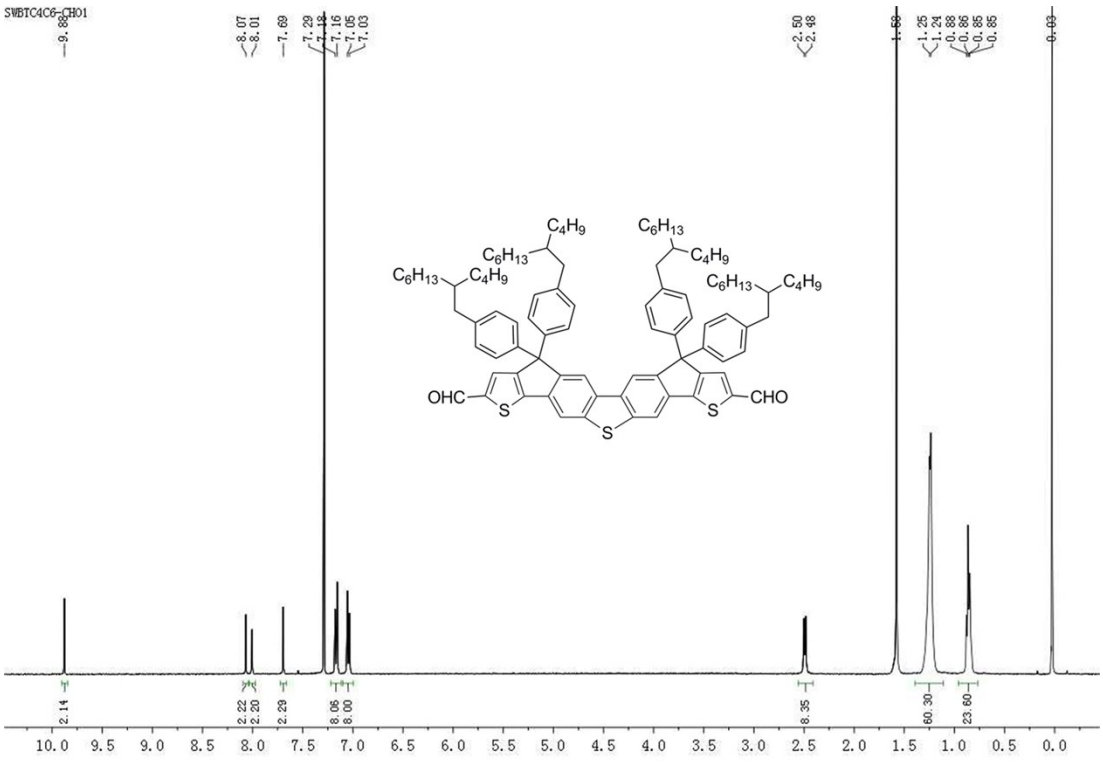

Fig. S11 ^{1}H NMR spectrum of compound **DBT-CHO**.

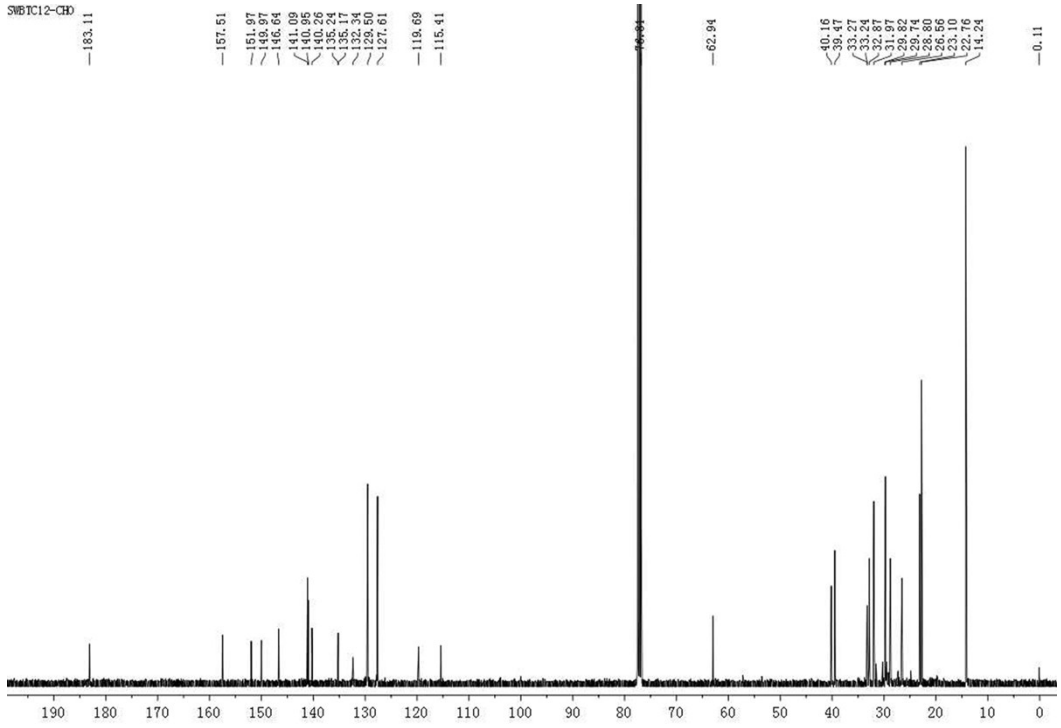

Fig. S12 ^{13}C NMR spectrum of compound **DBT-CHO**.

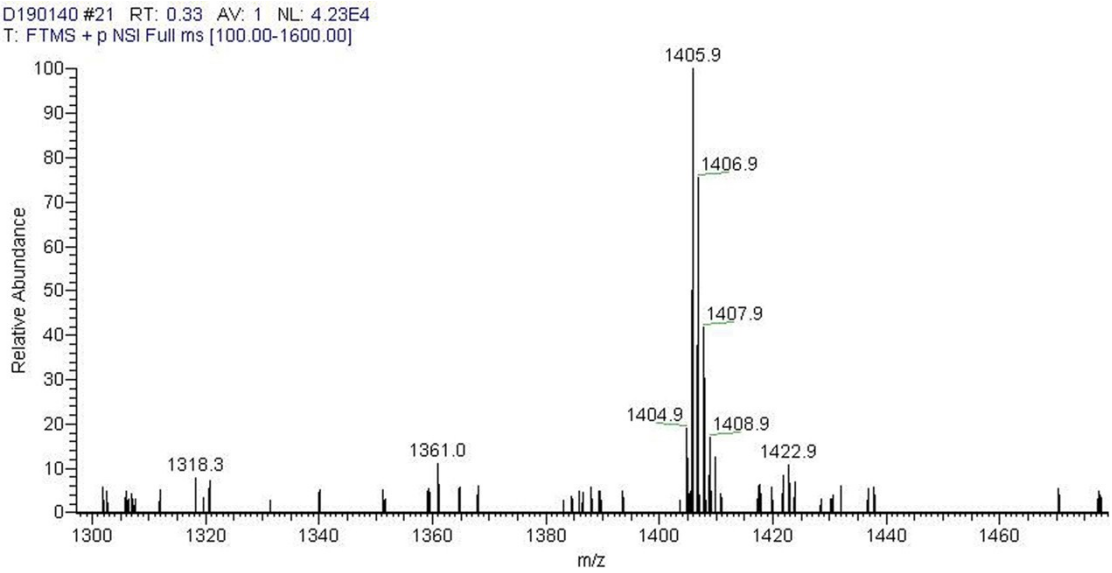

Fig. S13 MS spectrum of compound **DBT-CHO**.

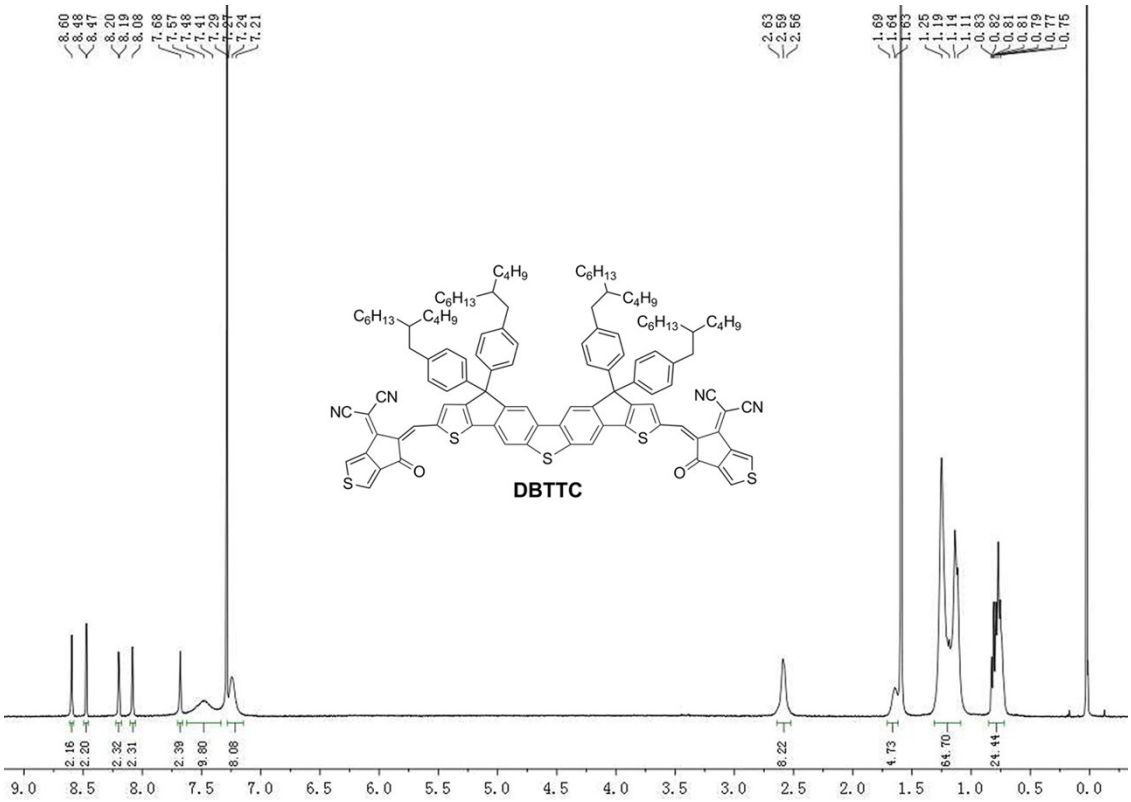

Fig. S14 ^{1}H NMR spectrum of compound **DBTTC**.

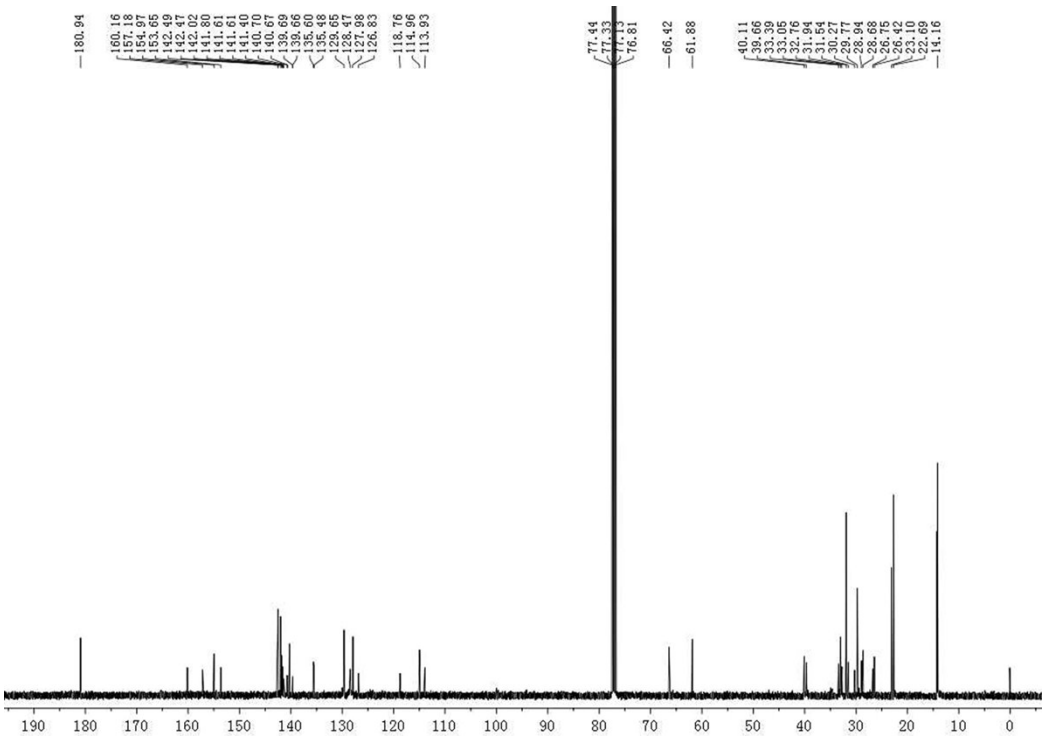

Fig. S15 ^{13}C NMR spectrum of compound **DBTTC**.

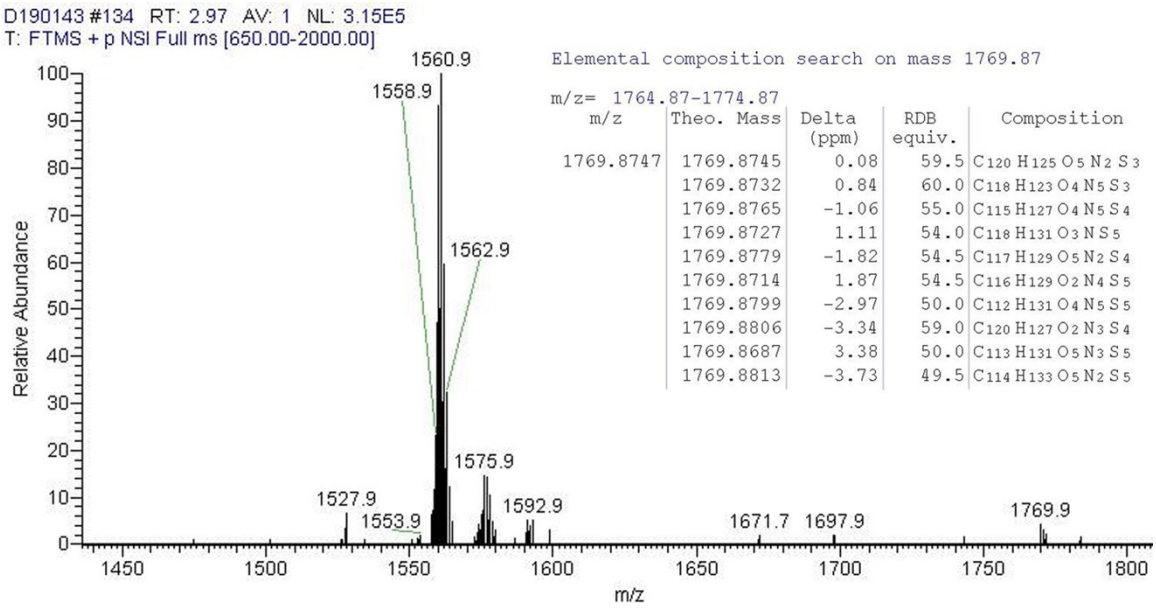

Elemental composition search on mass 1769.87

m/z= 1764.87-1774.87

m/z	Theo. Mass	Delta (ppm)	RDB equiv.	Composition
1769.8747	1769.8745	0.08	59.5	$C_{120}H_{125}O_5N_2S_3$
	1769.8732	0.84	60.0	$C_{118}H_{123}O_4N_5S_3$
	1769.8765	-1.06	55.0	$C_{115}H_{127}O_4N_5S_4$
	1769.8727	1.11	54.0	$C_{118}H_{131}O_3NS_5$
	1769.8779	-1.82	54.5	$C_{117}H_{129}O_5N_2S_4$
	1769.8714	1.87	54.5	$C_{116}H_{129}O_2N_4S_5$
	1769.8799	-2.97	50.0	$C_{112}H_{131}O_4N_5S_5$
	1769.8806	-3.34	59.0	$C_{120}H_{127}O_2N_3S_4$
	1769.8687	3.38	50.0	$C_{113}H_{131}O_5N_3S_5$
	1769.8813	-3.73	49.5	$C_{114}H_{133}O_5N_2S_5$

Fig. S16 HR-MS spectrum of compound **DBTTC**.

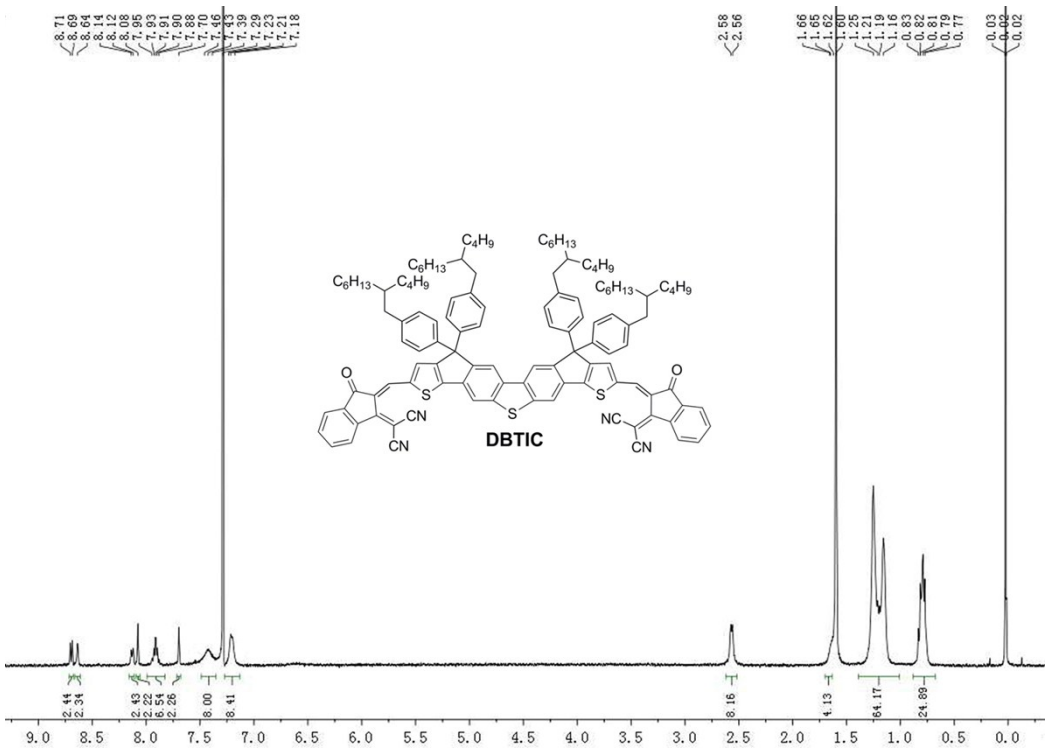

Fig. S17 ^{1}H NMR spectrum of compound **DBTIC**.

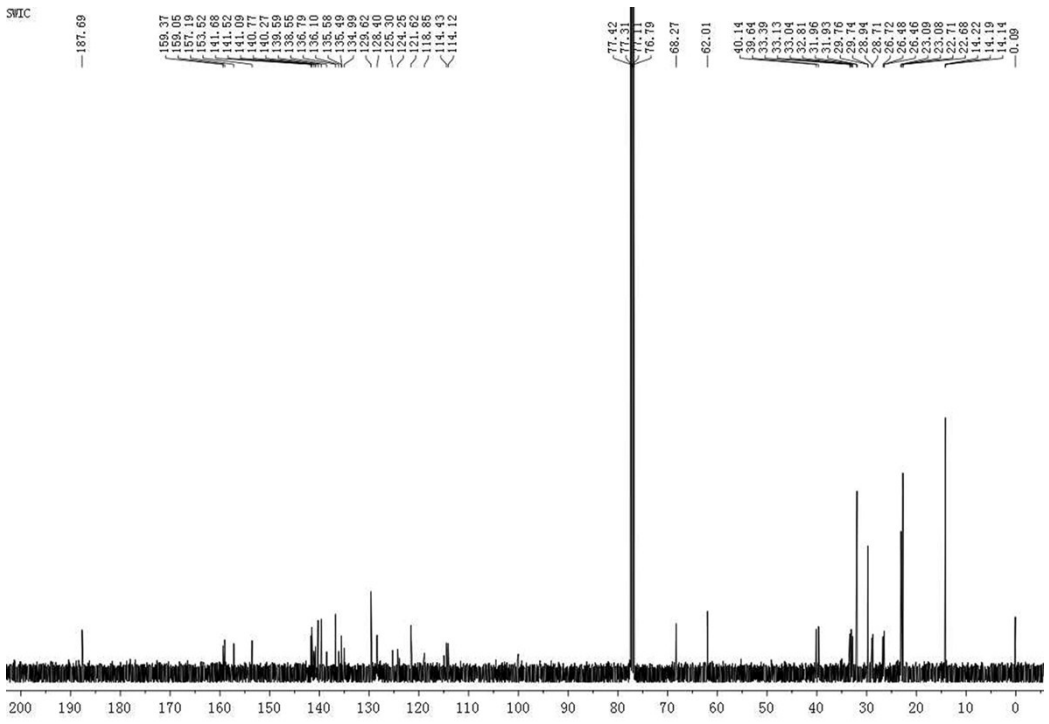

Fig. S18 ^{13}C NMR spectrum of compound **DBTIC**.

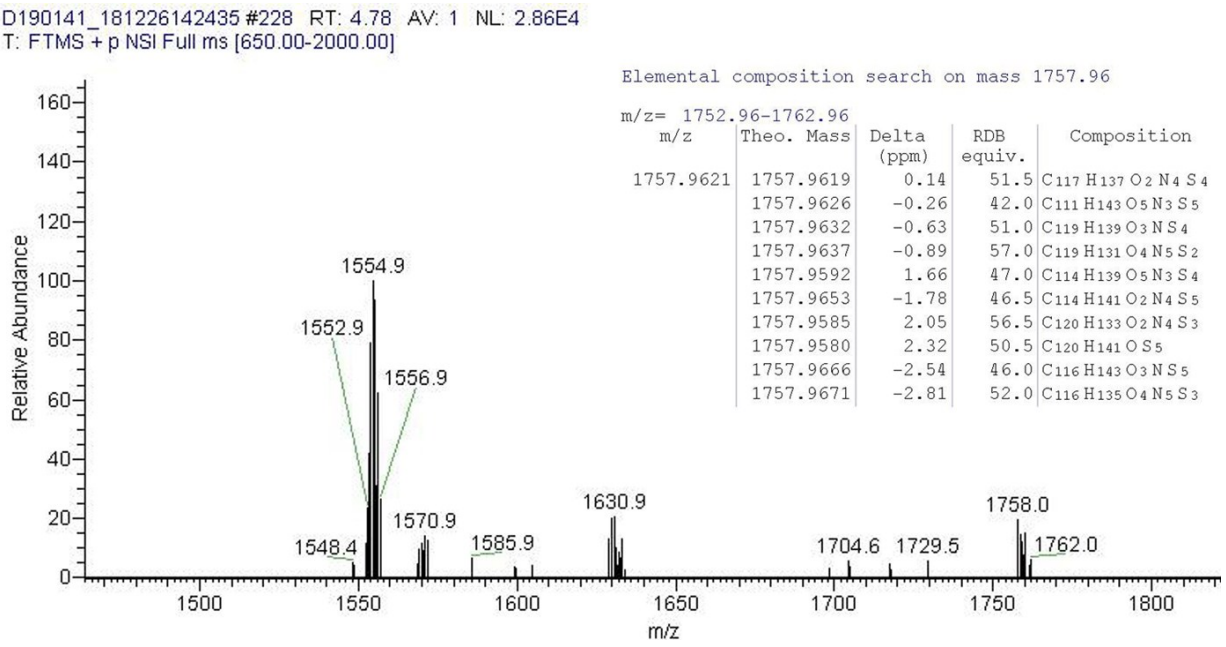

Elemental composition search on mass 1757.96

m/z= 1752.96-1762.96

m/z	Theo. Mass	Delta (ppm)	RDB equiv.	Composition
1757.9621	1757.9619	0.14	51.5	$C_{117}H_{137}O_2N_4S_4$
	1757.9626	-0.26	42.0	$C_{111}H_{143}O_5N_3S_5$
	1757.9632	-0.63	51.0	$C_{119}H_{139}O_3NS_4$
	1757.9637	-0.89	57.0	$C_{119}H_{131}O_4N_5S_2$
	1757.9592	1.66	47.0	$C_{114}H_{139}O_5N_3S_4$
	1757.9653	-1.78	46.5	$C_{114}H_{141}O_2N_4S_5$
	1757.9585	2.05	56.5	$C_{120}H_{133}O_2N_4S_3$
	1757.9580	2.32	50.5	$C_{120}H_{141}OS_5$
	1757.9666	-2.54	46.0	$C_{116}H_{143}O_3NS_5$
	1757.9671	-2.81	52.0	$C_{116}H_{135}O_4N_5S_3$

Fig. S19 HRMS spectrum of compound **DBTIC**.

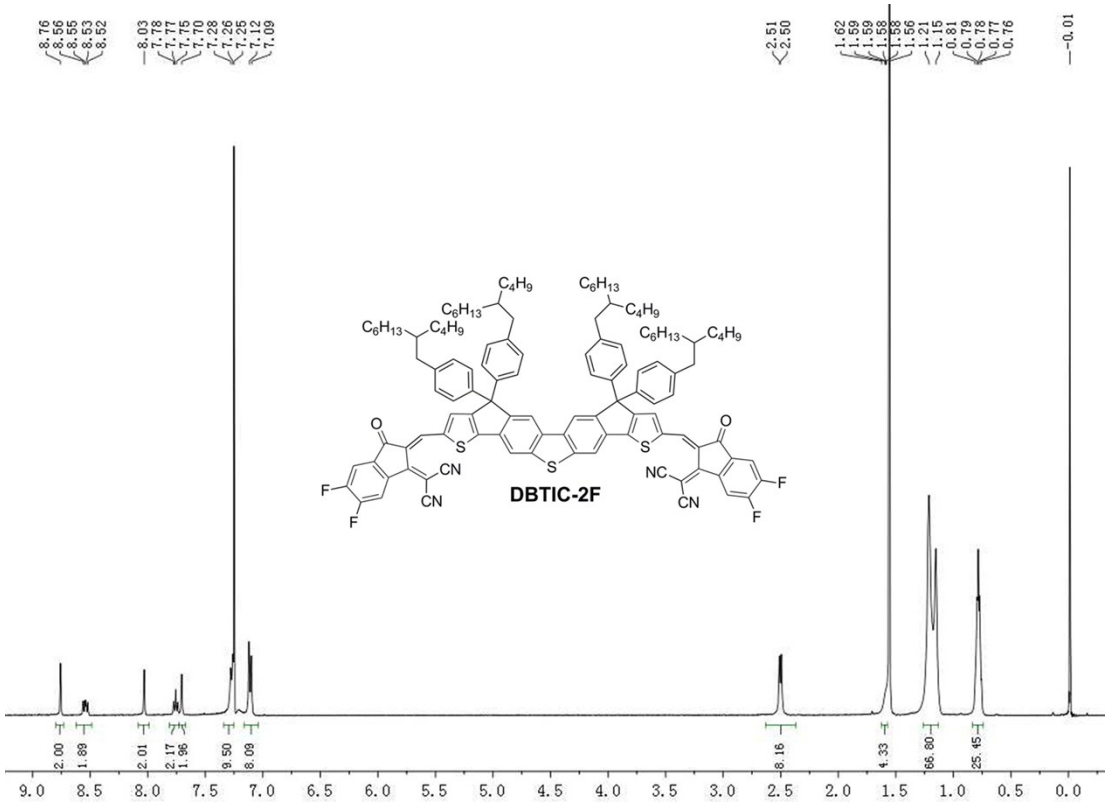

Fig. S20 ^{1}H NMR spectrum of compound **DBTIC-2F**.

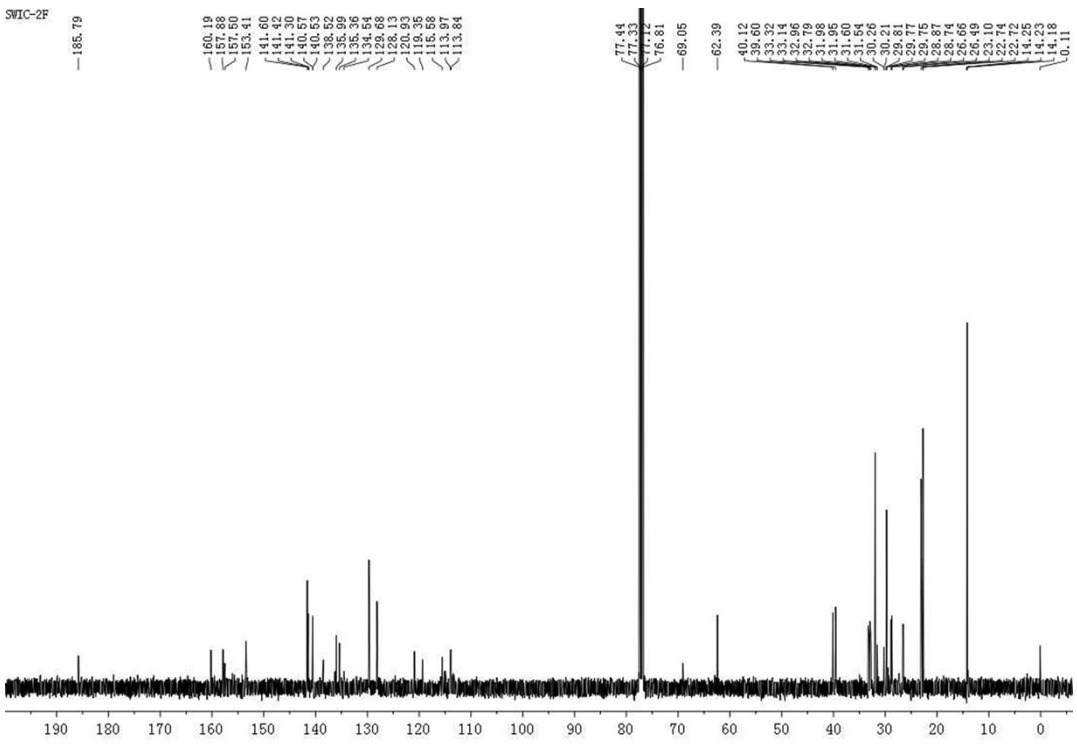

Fig. S21 ^{13}C NMR spectrum of compound **DBTIC-2F**.

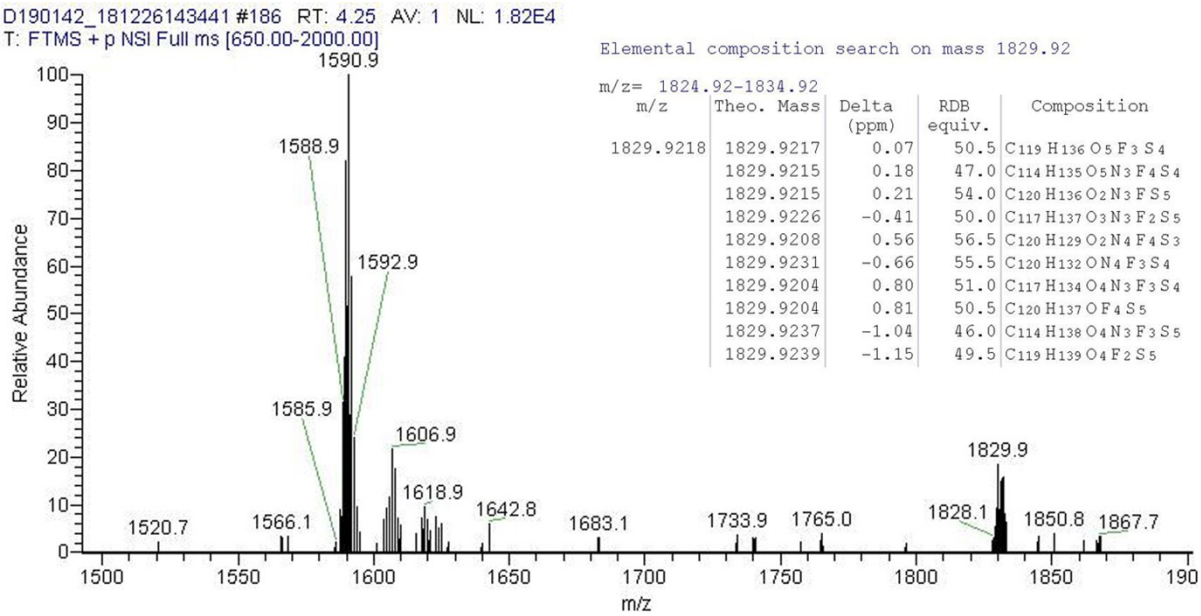

Elemental composition search on mass 1829.92

m/z= 1824.92-1834.92

m/z	Theo. Mass	Delta (ppm)	RDB equiv.	Composition
1829.9218	1829.9217	0.07	50.5	$C_{119}H_{136}O_5F_3S_4$
	1829.9215	0.18	47.0	$C_{114}H_{135}O_5N_3F_4S_4$
	1829.9215	0.21	54.0	$C_{120}H_{136}O_2N_3FS_5$
	1829.9226	-0.41	50.0	$C_{117}H_{137}O_3N_3F_2S_5$
	1829.9208	0.56	56.5	$C_{120}H_{129}O_2N_4F_4S_3$
	1829.9231	-0.66	55.5	$C_{120}H_{132}ON_4F_3S_4$
	1829.9204	0.80	51.0	$C_{117}H_{134}O_4N_3F_3S_4$
	1829.9204	0.81	50.5	$C_{120}H_{137}OF_4S_5$
	1829.9237	-1.04	46.0	$C_{114}H_{138}O_4N_3F_3S_5$
	1829.9239	-1.15	49.5	$C_{119}H_{139}O_4F_2S_5$

Fig. S22 HRMS spectrum of compound **DBTIC-2F**.